*J. Fluid Mech.* (2008), *vol.* 616, *pp.* 111–133. © 2008 Cambridge University Press 
doi:10.1017/S0022112008004084 Printed in the United Kingdom

# Steady inlet flow in stenotic geometries: convective and absolute instabilities

M. D. GRIFFITH[1,2]†, T. LEWEKE[2], M. C. THOMPSON[1] AND K. HOURIGAN[1]

[1]Fluids Laboratory for Aeronautical and Industrial Research (FLAIR), Department of Mechanical and Aerospace Engineering & Division of Biological Engineering, Monash University, Melbourne, Victoria 3800, Australia

[2]Institut de Recherche sur les Phénomènes Hors Equilibre (IRPHE), CNRS/Universités Aix-Marseille, 49 rue Frédéric Joliot-Curie, BP 146, F-13384 Marseille Cedex 13, France

(Received 15 October 2007 and in revised form 1 September 2008)

Steady inlet flow through a circular tube with an axisymmetric blockage of varying size is studied both numerically and experimentally. The geometry consists of a long, straight tube and a blockage, semicircular in cross-section, serving as a simplified model of an arterial stenosis. The stenosis is characterized by a single parameter, the aim being to highlight fundamental behaviours of constricted flows, in terms of the total blockage. The Reynolds number is varied between 50 and 2500 and the stenosis degree by area between 0.20 and 0.95. Numerically, a spectral-element code is used to obtain the axisymmetric base flow fields, while experimentally, results are obtained for a similar set of geometries, using water as the working fluid. At low Reynolds numbers, the flow is steady and characterized by a jet flow emanating from the contraction, surrounded by an axisymmetric recirculation zone. The effect of a variation in blockage size on the onset and mode of instability is investigated. Linear stability analysis is performed on the simulated axisymmetric base flows, in addition to an analysis of the instability, seemingly convective in nature, observed in the experimental flows. This transition at higher Reynolds numbers to a time-dependent state, characterized by unsteadiness downstream of the blockage, is studied in conjunction with an investigation of the response of steady lower Reynolds number flows to periodic forcing.

## 1. Introduction

Recent interest in the fluid mechanics associated with blood flow has largely stemmed from the identification of biological responses of arterial walls to fluid mechanical properties. In particular, the appearance and growth of arterial blockages, or stenoses, has been linked to the presence of low and oscillatory wall shear stresses (Ku 1997). For this reason, numerous researchers have studied the flow through models of stenotic arteries. These stenotic geometry studies have most often involved the investigation of pulsatile inlet flow (Ahmed & Giddens 1984; Ohja *et al.* 1989; Ahmed 1998; Stroud, Berger & Saloner 2002; Blackburn & Sherwin 2007; Varghese, Frankel & Fischer 2007*b*); however, the main focus of the study presented in this paper is the downstream flow due to steady Poiseuille upstream flow through a stenosis. The aim of the investigation is to provide a useful reference case of the flow generated by a pulsatile upstream flow, of which the steady inlet flow is a limiting case.

† Email address for correspondence: martin.griffith@eng.monash.edu.au

https://doi.org/10.1017/S0022112008004084 Published online by Cambridge University Press

Cassanova & Giddens (1978) reported on the flow through contoured and sharp-edged stenoses, creating experimentally a steady inlet flow through a smooth stenosis modelled as a cosine. They observed and described disturbance in the flow downstream of a constriction of 75% area reduction for Reynolds number $Re = 635$. The work presented in Cassanova & Giddens (1978) continues in Ahmed & Giddens (1983*a*, *b*). Using laser Doppler anemometry, velocity profiles were measured for stenosis severities of 25%, 50% and 75% area reduction and for Reynolds numbers 500, 1000 and 2000. Discrete frequency oscillations for $Re = 500$ were observed, while for $Re = 1000$ and 2000, they observed similar oscillations, this time with turbulence in the region further than four diameters downstream of the stenosis. No critical Reynolds numbers for instability were presented; only observations of unsteadiness and turbulence at the Reynolds numbers were tested.

More recently, numerical work on the steady inlet flow through a cosine stenosis of area reduction 75% has been carried out by Sherwin & Blackburn (2005). They determined a critical Reynolds number of 722 from a linear stability analysis of the flow. The leading perturbation mode (azimuthal wavenumber $m = 1$) consisted of a loss of symmetry of the jet. This deflection of the centreline of the jet was described as promoting a 'mild Coanda-type attachment'. Direct numerical simulation of the three-dimensional flow for $Re = 750$ revealed the instability to be subcritical; hysteresis was confirmed with the instability being observed down to $Re = 688$. The asymptotic flow displayed a long-period oscillation, with the beginning of the turbulent region of the flow oscillating between axial locations four and ten diameters downstream of the stenosis.

Sherwin & Blackburn (2005) asserted that the instability in the direct numerical simulation for $Re = 750$ – along with the hysteresis – was consistent with the instabilities seen in the experimental works of Cassanova & Giddens (1978) and Ahmed & Giddens (1983*b*). Critical Reynolds numbers were not reported in the experimental works. Instability was reported as beginning between $Re = 500$ and $Re = 1000$; however, it was described as discrete frequency oscillations. It would appear that even though the critical Reynolds number reported in Sherwin & Blackburn (2005) (and its lower subcritical value) is consistent with the Reynolds numbers for instability in the experimental work of Cassanova & Giddens (1978) and Ahmed & Giddens (1983*b*), the causes of the instabilities are perhaps different. In the earlier experimental work, the observed instabilities seemed to be convective and dependent on the experimental noise; for the numerical simulations of Sherwin & Blackburn (2005), the initial bifurcation of instability was absolute.

Convective instability seems to play an important role in stenotic flows with steady inlet flow; therefore, in an extension of their earlier work, Blackburn & Sherwin (2007) investigated the response of their steady flow simulations to a periodic forcing applied at the flow inlet. The response of the flow to the forcing manifested as a roll-up of the shear layer into discrete vortices. This form of instability was more consistent with the type of disturbance seen in Cassanova & Giddens (1978) and Ahmed & Giddens (1983*b*). Blackburn & Sherwin (2007) also quantified the response of the flow at different forcing periods by calculating the extra kinetic energy generated by the forcing. For $200 < Re < 700$, they found a maximum response to forcing at a non-dimensionalized period $T\overline{U}/D \approx 0.4$, where $T$ is the forcing period, $D$ the tube diameter and $\overline{U}$ the average fluid velocity in the unblocked tube.

Varghese, Frankel & Fischer (2007*a*) conducted direct numerical simulations of the steady inlet flow for Reynolds numbers of 500 and 1000, through a smooth axisymmetric stenosis, the same as that used in previous experiments by Ahmed &

https://doi.org/10.1017/S0022112008004084 Published online by Cambridge University Press

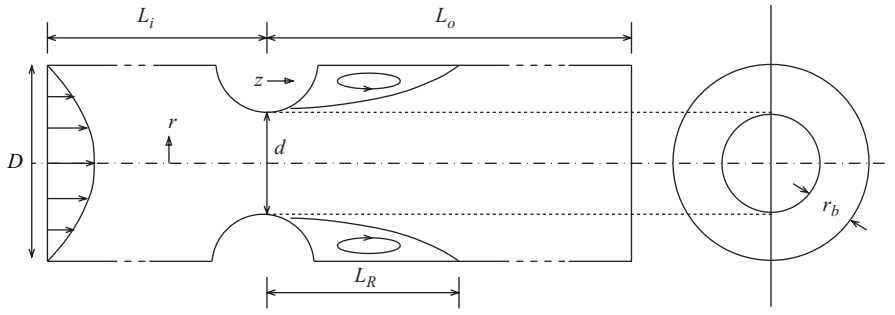



FIGURE 1. Schematic of the geometry.

Giddens (1983*b*). In contrast to the experiments, they found that the jet emanating from the stenosis remained laminar for both the Reynolds numbers tested. However, the introduction of a 5 % eccentricity to the stenosis geometry created a perturbation which resulted in a turbulent flow downstream that matched more closely the experiments of Ahmed & Giddens (1983*b*) and Cassanova & Giddens (1978). The presence of a similar turbulent breakdown of the flow, triggered in one case by a geometric eccentricity and in the other by experimental noise, suggests an independence of the structure of the turbulent breakdown from the mechanism which triggers it.

The need for a geometric perturbation in the work of Varghese *et al.* (2007*a*) to produce results comparable to experiments and the study of shear layer response to periodic forcing in Blackburn & Sherwin (2007) hint at the role of convective instability in steady stenotic flow, providing an avenue of inquiry still to be explored.

The aim of this paper is to explore the effect on flow behaviour of a variation of the stenosis degree of the geometry. In effect, such a variation tracks the development of an arterial stenosis from its genesis to its more pathological states. To make the problem more tractable and at the same time more applicable as a useful base case, it was felt prudent to reduce the stenosis geometry to a single parameter. This provides us with a well-defined parameter space. As well as being a simpler problem to analyse, the geometry allows comparisons to be drawn with previous work on flows past cylinders. Thus far, the effect on the flow of changes in stenosis degree is not something that has been dealt with in great depth in the literature. The flows reported in this article are modelled numerically and experimentally. This allows observation of the relations and differences between real flows (with the effects of background noise and small asymmetries) and those simulated numerically.

The following section gives a more precise definition of the problem under consideration, followed by a description of the methods employed in the study. In § 4, we detail the results of the analysis, followed by conclusions in § 5.

## 2. Problem definition

The geometry under investigation is shown in figure 1. It consists of a long straight tube with an axisymmetric blockage described by a single parameter, the stenosis degree, defined as

$$b = 1 - \left(\frac{d}{D}\right)^2, \tag{2.1}$$

where $D$ is the diameter of the tube and $d$ is the diameter at the centre of the blockage. Figure 1 also shows the radius of the blockage, dependent on $d$, which can

https://doi.org/10.1017/S0022112008004084 Published online by Cambridge University Press

be defined as

$$r_b = \frac{D-d}{2} = \frac{D}{2}(1-\sqrt{1-b}). \tag{2.2}$$

In *in vivo* blood flow, artery walls are compliant and respond to the fluid pressure and wall shear stresses. The walls of the tube of our model are considered to be rigid. As well as greatly simplifying our problem, the effect of compliant walls is generally considered negligible for the study of flows in larger arteries (Ku 1997; Wootton & Ku 1999). Similarly, for larger arteries, it is generally reasonable to assume the fluid to be Newtonian. The Reynolds number is defined as

$$Re = \frac{\overline{U}D}{\nu}, \tag{2.3}$$

where $\overline{U}$ is the sectionally averaged fluid velocity, $D$ the tube diameter and $\nu$ the kinematic viscosity. The coordinate system is such that the origin ($r=0$, $z=0$) is located on the centreline of the tube at the axial mid-point of the stenosis. We examine flows ranging from Reynolds number values of 50 to 2500 with stenosis degree from 0.2 to 0.95.

## 3. Method

The study employs both numerical and experimental methods.

### 3.1. *Numerical simulations*

Two-dimensional axisymmetric flow field simulations were obtained from a numerical solution of the time-dependent Navier–Stokes equations, given here with the incompressibility constraint,

$$\frac{\partial \overline{\boldsymbol{u}}}{\partial t} + \overline{\boldsymbol{u}} \cdot \nabla \overline{\boldsymbol{u}} = -\nabla \overline{p} + \nu \nabla^2 \overline{\boldsymbol{u}}, \tag{3.1}$$

$$\nabla \cdot \overline{\boldsymbol{u}} = 0, \tag{3.2}$$

where $\overline{\boldsymbol{u}}$ is the three-dimensional velocity vector (solved axisymmetrically), and $\overline{p}$ and $\nu$ are the kinematic pressure and viscosity, respectively. The simulations were initialized with the fluid at rest and run until the flow had achieved a converged and steady state. The spectral-element method employed to discretize and solve the equations has been used and validated in the prediction of wake flows past rings (Sheard, Thompson & Hourigan 2003), spheres (Thompson, Leweke & Provansal 2001) and circular cylinders (Thompson, Hourigan & Sheridan 1996). The method uses a three-step time-splitting procedure and has been verified to give second-order time accuracy (Karniadakis, Israeli & Orszag 1991). On the stenosis surface and the cylinder walls, no-slip conditions were imposed. At the inlet boundary, an equilibrium Poiseuille profile was prescribed. At the outflow boundary far downstream, the standard zero normal velocity gradient condition was imposed.

Linear stability analysis is carried out on the numerically simulated flows. The method analyses the growth, or decay, of a perturbation, $\boldsymbol{u}'(r,\theta,z,t)$, on the steady base flow, $\overline{\boldsymbol{u}}(r,\theta,z)$. Describing the flow as the steady and perturbation components combined, this definition is substituted into the Navier–Stokes equations. Subtracting the base flow components and removing nonlinear terms yields linear equations describing the evolution of small disturbances, which can be solved by the same numerical method used to solve the base flow. For a given azimuthal wavenumber, $m$, the maximum growth rate $\sigma$ (normalized by $\overline{U}/D$) is then determined by the power

https://doi.org/10.1017/S0022112008004084 Published online by Cambridge University Press

| | $Re = 2000$, $b = 0.5$ | | $Re = 800$, $b = 0.75$ | | $Re = 500$, $b = 0.9$ | |
|---|---|---|---|---|---|---|
| $n$ | $L_R/D$ | $\sigma$ | $L_R/D$ | $\sigma$ | $L_R/D$ | $\sigma$ |
| 5 | 7.413 | −0.012536 | 18.398 | 0.0037702 | – | – |
| 6 | 7.362 | −0.014418 | 18.378 | 0.0032027 | 41.399 | 0.0085549 |
| 7 | 7.353 | −0.014795 | 18.376 | 0.0031348 | 41.401 | 0.0083672 |
| 8 | 7.355 | −0.014779 | 18.375 | 0.0031348 | 41.404 | 0.0083672 |
| 9 | 7.356 | −0.014783 | 18.377 | 0.0031348 | 41.405 | 0.0083752 |

TABLE 1. Convergence of the normalized initial recirculation length, $L_R/D$, and maximum growth rate, $\sigma$, across three stenosis degrees with increasing polynomial order.

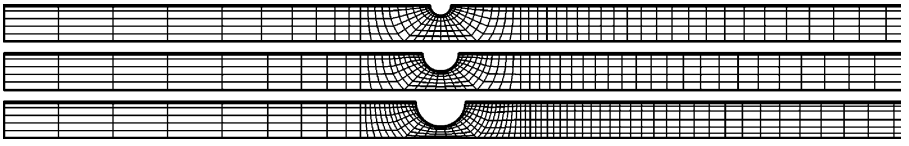


FIGURE 2. Macroelement meshes constructed for $b = 0.5$, 0.75 and 0.9 (top to bottom). Only the portions up to $z/D = 6$ are shown.

method. The method is the same one used in Griffith *et al.* (2007), only modified for axisymmetric configurations.

### 3.1.1. *Mesh layout and resolution*

Seven meshes were constructed at stenosis degrees of $b = 0.2$, 0.4, 0.5, 0.6, 0.75, 0.9 and 0.95. Figure 2 shows the test sections of three meshes at $b = 0.5$, 0.75 and 0.9. The same macroelement resolution was retained across the stenosis degree range; however, it was found that at the higher end of the range, a greater resolution was required. Of course, this is not surprising given the increased velocity gradients caused by the fluid squeezing through ever-smaller throats. The same basic mesh layout was used for each grid, with the macroelement distribution more highly concentrated near the cylinder walls and throughout and immediately downstream of the stenosis. The resolution was decreased downstream of the outlet boundary. Functions are represented internally by $(n-1) \times (n-1)$ tensor product Lagrangian polynomials in local computational space. The functions are fit using $n \times n$ internal nodes, distributed according to the Gauss–Legendre–Lobatto integration points. An advantage of the approach is the ability to set the polynomial order at run-time, allowing resolution studies to be performed more easily.

A grid resolution study was undertaken. The final internal grid resolution used for most simulations was $n = 7$, or 49 nodes per element, with no marked differences observed between predictions from simulations at this resolution and those for $n = 6$. For larger blockages and Reynolds numbers, elements of order $n = 8$, comprising 64 nodes per element, were employed to properly resolve the more strongly varying regions of the flow field. Convergence tests were performed on three of the meshes, the first one at $b = 0.5$, $Re = 2000$, the second one at $b = 0.75$, $Re = 800$ and the third one at $b = 0.9$, $Re = 500$, the results of which are shown in table 1. The table plots the convergence of the growth rate of the most unstable mode number from the linear stability analysis, outlined in § 3.1, and of the normalized length of the steady recirculation zone, which appears in the flow immediately downstream of the stenosis. The inlet length used for all meshes was $L_i = 6D$, which was found to be sufficient

https://doi.org/10.1017/S0022112008004084 Published online by Cambridge University Press

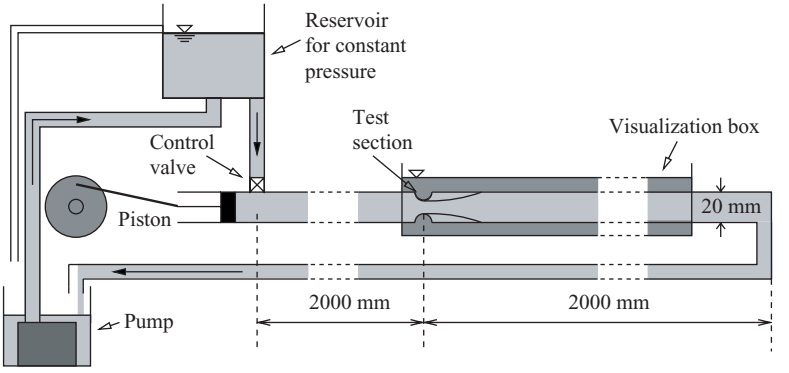



FIGURE 3. Schematic of the experimental rig; the inlet and outlet lengths have been truncated.

to remove any effect of the inlet length on the downstream flow. The outlet length, $L_o$, was varied according to the stenosis degree. For low stenosis degree, the outlet length used was $40D$, increasing to $50D$ for $b = 0.6$, $75D$ for $b = 0.75$ and $100D$ for $b = 0.9$. The effect of a change in outlet length was investigated. For a mesh of outlet length $L_o = 175D$ for $b = 0.9$ and $Re = 400$ and another of $L_o = 150D$ for $b = 0.75$ and $Re = 1000$, simulations were performed to compare to those obtained by using meshes of shorter outlet lengths. These tests established that only negligible differences on the upstream flow were present when the shorter outlet lengths were employed.

### 3.2. *Experimental method*

An experimental rig was constructed to test the geometry outlined in figure 1. A schematic of the rig design is shown in figure 3. (Further details of the experimental rig are provided in Griffith 2007.) The rig consisted of a transparent perspex tube of 20 mm diameter, with inlet and outlet lengths of 2000 mm or $100D$. This provided a fully developed Poiseuille flow at the test section and restricted any end effects. The three removable test sections constructed corresponded to stenosis degrees of $b = 0.5$, 0.75 and 0.9. The test section and outlet length were contained in a rectangular water-filled viewing box, which allowed a largely undistorted view of the flow in the tube. A pump supplied an elevated water reservoir, thereby keeping the pressure in the system constant. The Reynolds number was varied via a control valve located before the entry into the inlet tube.

A piston was added at the junction immediately downstream of the control valve. This piston allowed the investigation of flows subject to a high-frequency forcing, as discussed in § 4.2.2. In addition, although not discussed in this paper, the piston could generate pulsatile flows, that is flows comprising of a steady flow with a large-amplitude periodic pulse added. At running conditions, the pressure drop across the control valve was very large, thus ensuring that movement from the piston was translated directly downstream and only a negligible portion lost upstream to the reservoir.

Much effort was invested in reducing the noise and vibration in the system: the water pump and piston were isolated as much as possible; the straightness of the tube was ensured, and filters were placed to smooth the flow before its entry into the inlet section. The turbulence intensity (standard deviation of the velocity divided by the mean velocity) of the unblocked flow in the rig was measured. Using series of 140 particle image velocimetry image pairs, a turbulence intensity of 3% along the centreline of the tube was obtained, reaching a converged value after approximately 100 image pairs.

https://doi.org/10.1017/S0022112008004084 Published online by Cambridge University Press

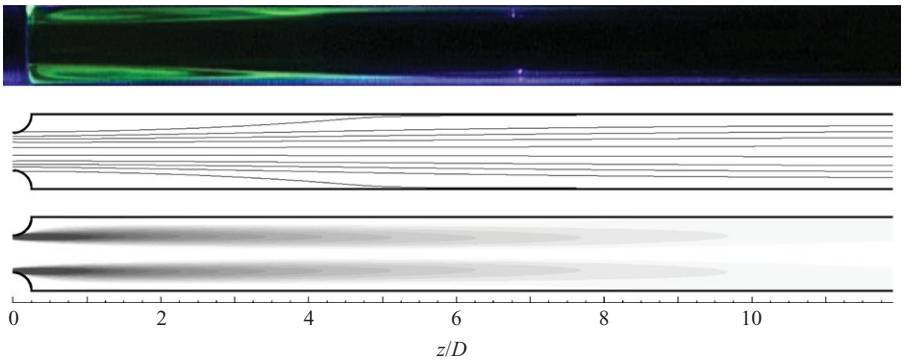



FIGURE 4. Comparison between the dye visualization, numerical streamlines and vorticity (top to bottom), at $b = 0.75$ and $Re = 194$. In the dye visualization, a reflection of the laser in the middle of the image on the bottom portion of the tube is present, evident in the figure as a thin, blue shade. Flow is from left to right.

The flow was analysed primarily using coloured dye visualizations. Fluoroscein dye was injected into the flow immediately downstream of the stenosis, allowed to settle and then illuminated by a laser sheet. This technique was most useful in visualizing the recirculation zone and shear layer of the separated flow. The dye trapped in a steady recirculation zone contrasted with the dye-free fluid arriving from upstream.

## 4. Results

### 4.1. *Steady flow*

Figure 4 depicts the generic flow structure under investigation for $b = 0.75$ and $Re = 194$. For this Reynolds number, the flow is laminar and steady. Experimentally, a recirculation zone is evident from the dye trapped immediately downstream of the stenosis; the rest of the dye in the mainstream flow is convected away. For low Reynolds numbers, the dye remains in the recirculation zone long after the injection period. A comparison is made with streamlines and the vorticity field taken from an equivalent numerical simulation. The recirculation zone is again apparent, this time by the separating streamline. The flow can be characterized as a confined jet emanating from the constriction, which expands downstream of the stenosis. A long, thin shear layer is created by the detachment of the flow on the downstream half of the stenosis. As the Reynolds number is increased, the length of the recirculation zone downstream of the stenosis increases. Figure 5 shows streamlines for simulated flows at a range of Reynolds numbers for $b = 0.5$. Across the stenosis degree range, the length of the recirculation zone increases linearly with Reynolds number. The recirculation zone is long and thin, with the neutral streamline running nearly parallel to the tube wall.

The length of the recirculation zone $L_R$ behind the stenosis serves as a useful means to characterize the flow. Figure 6($a$) shows the lengths across the stenosis range tested numerically as a function of Reynolds number. The recirculation length can be measured either by locating the point at which the separating streamlines meet the wall or by finding the point at which the wall shear stress is equal to zero. From figure 6($a$), we see a linear dependence of the recirculation length on Reynolds number, with the lengths at the higher end of the range increasing more rapidly. Indeed, above $b \approx 0.6$, the length increases sharply with stenosis degree when compared to the lower end of the range. This is not surprising, if we consider the increase in velocity through each of

https://doi.org/10.1017/S0022112008004084 Published online by Cambridge University Press

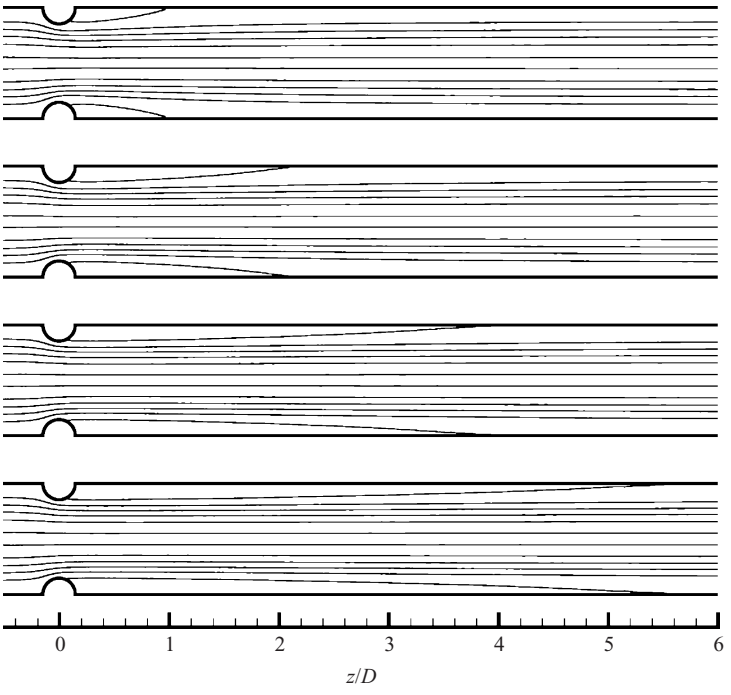



FIGURE 5. Streamlines at $b = 0.5$ and $Re = 200$, 500, 1000 and 1500. The terminating streamline indicates the recirculation length.

the stenosis degrees. The velocity ratio at $b = 0.95$ of $\overline{U}_{(z=0)}/\overline{U} = 20$ is enormous when compared to the equivalent values of 1.25 and 1.67 for $b = 0.2$ and 0.4, respectively.

Clearly of interest is the possible existence of a relation between the different data sets for each stenosis degree – presumably in the form $L_R/D = f(b)Re$. To this end, an analogy is drawn between the present work and the wake behind a circular cylinder at low Reynolds number, before shedding occurs. Knowing that the length of the recirculation zone behind a circular cylinder varies linearly with the Reynolds number of that flow ($Re_{cyl} = U_f 2r_b/\nu$, where $U_f$ is the free stream velocity, and $r_b$ is the radius of the stenosis blockage; Taneda 1956) and that the fluid velocity through the contraction is analogous to the free stream velocity for the cylinder flow ($U_f = \overline{U}/(1-b)$), we can write

$$\frac{L_R}{D} = \frac{L_R}{r_b} \cdot \frac{r_b}{D} \propto \frac{r_b}{D} \cdot Re_{cyl} \tag{4.1}$$

or

$$\frac{L_R}{D} = C\left(\frac{2r_b^2}{D^2(1-b)} \cdot Re\right), \tag{4.2}$$

where $C$ is a constant. Using (2.2), this can be expressed in terms of $b$ as

$$\frac{L_R}{D} = C\left(\frac{1}{1-b}\left(1-\frac{b}{2}\right) - \frac{1}{\sqrt{1-b}}\right) Re. \tag{4.3}$$

In order to test the comparison, we divide the recirculation lengths of figure 6(*a*) by the multiplier $([1/(1-b)](1-b/2) - 1/\sqrt{1-b})$ in (4.3), which gives the scaled

https://doi.org/10.1017/S0022112008004084 Published online by Cambridge University Press

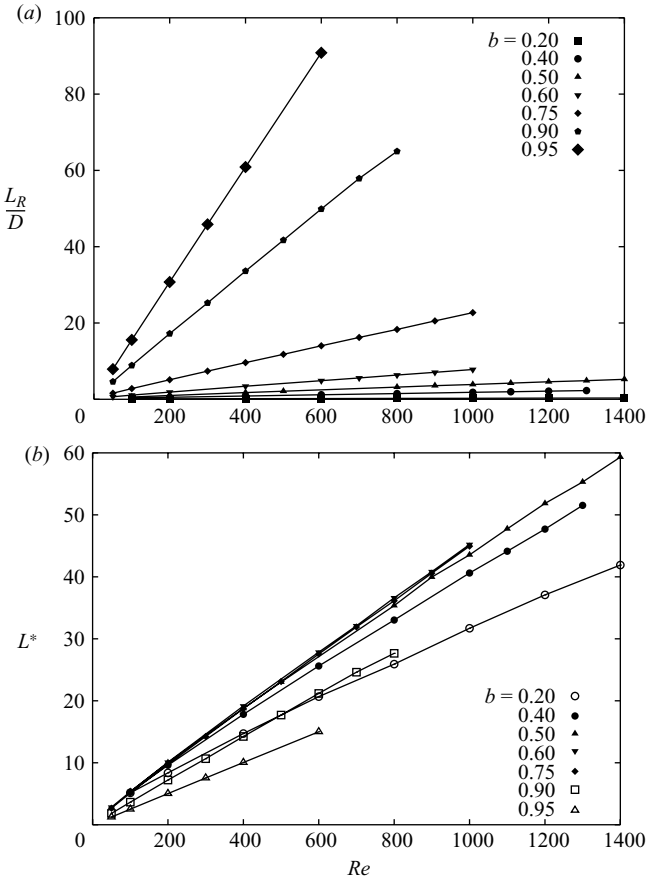



FIGURE 6. (*a*) Recirculation zone lengths as a function of Reynolds number and (*b*) $L^*$, the result of the scaling described in (4.3). A comparison with recirculation lengths measured from experimental results is presented in figure 13.

recirculation length $L^*$ shown in figure 6(*b*). Away from the extremes of the stenosis degree, there is a good collapse of the data for the intermediate values of stenosis degree, showing that the analogy is a good one. For $b = 0.2$, the stenosis consists of a small bump on the tube wall, with $r_b = 0.0528$. At this height, the local fluid velocity is also very small, with the fluid velocity decreasing quickly as we move closer to the wall. The greater part of the main fluid flow passes by the stenosis, not perturbed by the extent of the flows through the larger stenoses. The difference in the flow conditions local to the stenosis may account for the behaviour. For $b = 0.9$ and 0.95, there is also a divergence. These two cases are extreme, with the flow exhibiting a strong acceleration through the stenosis in relation to the other geometries. At this end of the scale, the flow features begin to approach those of a jet entering a quiescent fluid, rather than those of a tube with a mild contraction. This can be further seen in figure 7, where the relation shown in (4.3) is compared with the measured values. The constant C was chosen to be equal to 0.048, the value matching closely the gradient in figure 6(*b*). The dotted lines, plotting (4.3), match well with the measured values, up to the geometry corresponding to $b = 0.75$, beyond which the analogy loses applicability.

https://doi.org/10.1017/S0022112008004084 Published online by Cambridge University Press

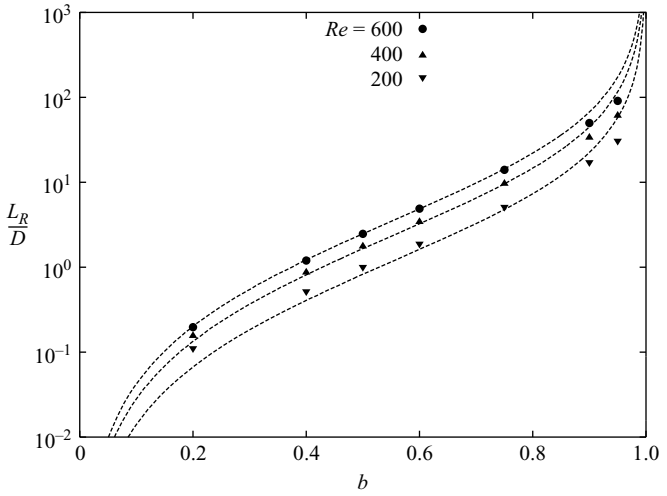



FIGURE 7. Variation of $L_R/D$ with stenosis degree, at $Re = 200$, 400 and 600. Dotted lines are plots of $L_R/D$ according to (4.3), with the constant $C$ set to 0.048.

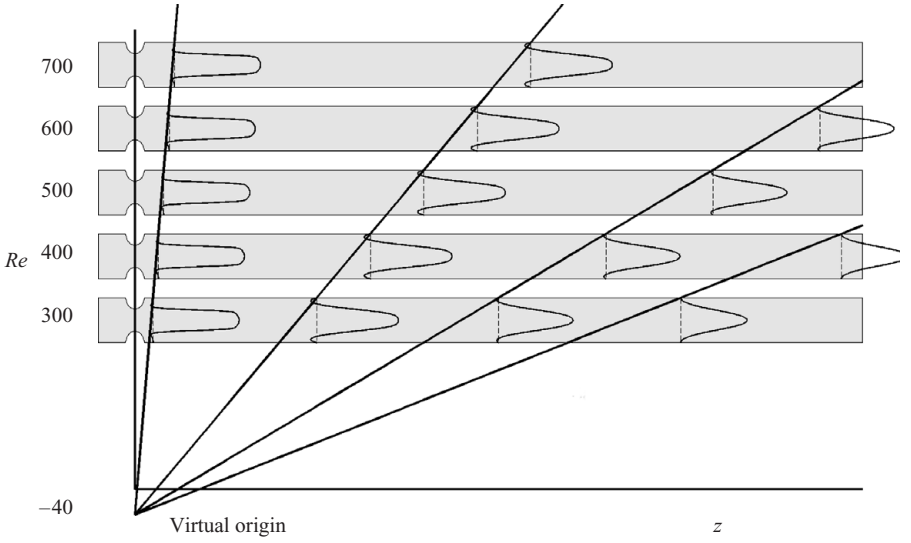



FIGURE 8. Graph showing similarity between profiles at different Reynolds numbers at $b = 0.75$. Across the Reynolds number range, the profiles are identical along the straight lines in the figure, all of which have an origin at $z = 0$ and $Re = -40$.

In a vein similar to the strongly linear behaviour seen in the recirculation length variation (figure 6) is the presence of similarities across the Reynolds number range. For $b = 0.75$, figure 8 shows plots of velocity profiles at various axial locations and a range of Reynolds numbers. By using the plotted lines in figure 8 and knowing the velocity field at one Reynolds number, the flow for another Reynolds number can be constructed. The profiles along the lines plotted are always identical. It is only closer to the contraction that the similarity is not as strong; however, even then the differences between the profiles are negligible. The strongly linear behaviour is in keeping with the linear behaviour seen in figure 6(*a*).

https://doi.org/10.1017/S0022112008004084 Published online by Cambridge University Press

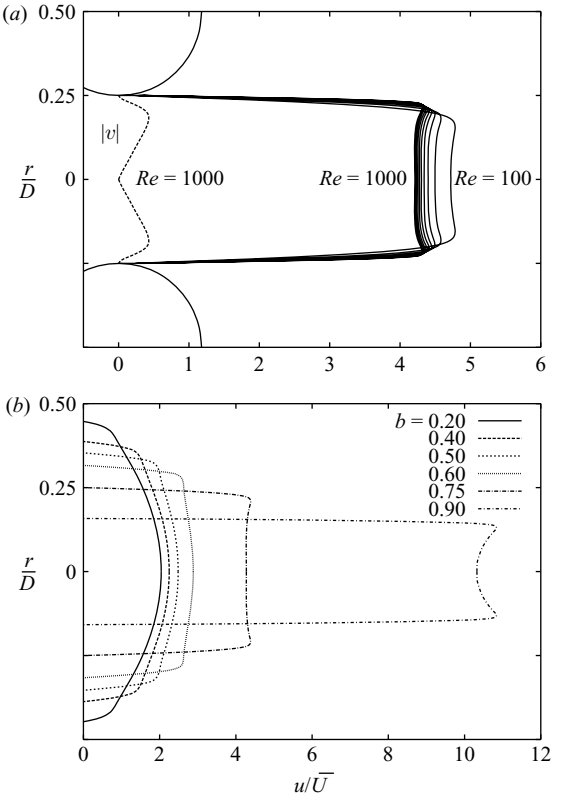



FIGURE 9. (*a*) Axial velocity profiles in the contraction of the $b = 0.75$ geometry, from $Re = 100$–$1000$, including a profile of absolute radial velocity, $|v|$, at $Re = 1000$. (*b*) Profiles in the contraction across the stenosis degree range, all at $Re = 600$.

The variation of the profiles within the contractions, at $z = 0$, is shown in figure 9. From figure 9(*a*), we see that the profiles take an unexpected shape. Rather than $u$ being at its maximum value in the middle of the tube, the maximum axial velocity is found at a radial location near $r/D \approx 0.75((D/2) - r_b)$, depending on Reynolds number. At high Reynolds numbers, the boundary layer formed over the stenosis surface is thinner; therefore we find the local maximum of axial velocity closer to the tube wall; at low Reynolds numbers, the thicker boundary layer pushes the local maximum closer to the tube axis. Also shown in figure 9(*a*) is a single profile of absolute radial velocity $|v|$. This velocity, $v$, is generated by the fluid moving to the centre to squeeze through the rapid contraction.

In comparison to many other studies of stenotic geometries (Deplano & Siouffi 1999; Stroud, Berger & Saloner 2000; Long *et al.* 2001; Mallinger & Drikakis 2002; Sherwin & Blackburn 2005), the present geometry consists of a more rapid contraction of the flow. This creates somewhat blunter profiles within the contraction and, at higher stenosis degree, a local maximum of velocity located very close to the stenosis wall. This observed difference can be seen in the profiles plotted in figure 9(*a*) and those presented for the throat of the stenosis in the works of both Ahmed & Giddens (1983*b*) and Varghese *et al.* (2007*a*). In these studies, which used a longer stenosis length, throat velocity profiles were blunt but did not exhibit the local maximum of axial velocity away from the tube centreline. The short stenosis length also creates

https://doi.org/10.1017/S0022112008004084 Published online by Cambridge University Press

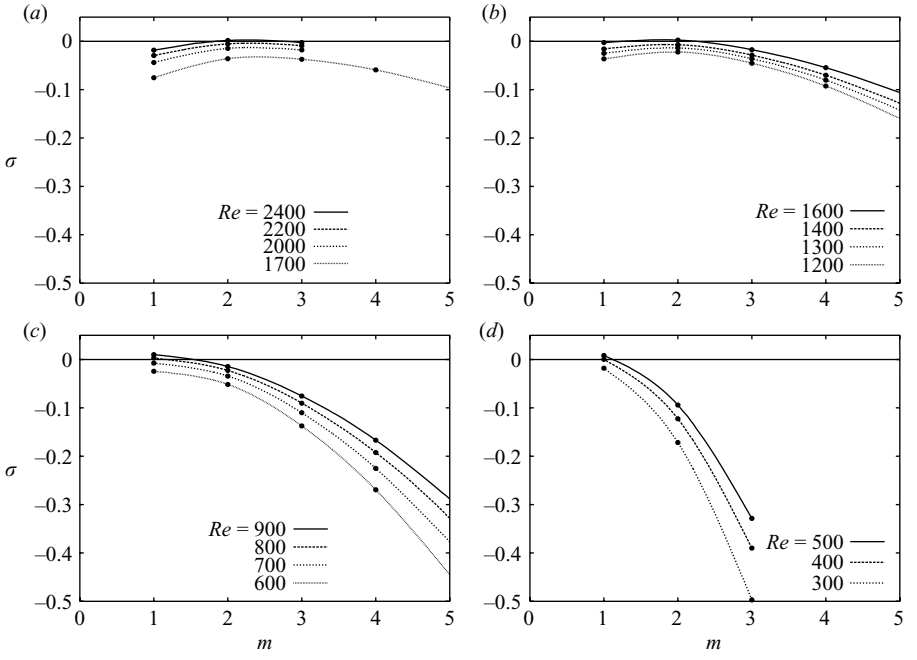



FIGURE 10. Plots of growth rates against azimuthal mode number, $m$, for absolute linear stability for $b = 0.5$, 0.6, 0.75 and 0.9. Lines have been drawn between the points to delineate the different Reynolds numbers. (*a*) $b = 0.5$; (*b*) $b = 0.6$; (*c*) $b = 0.75$; (*d*) $b = 0.9$.

thinner downstream separating shear layers than those seen in geometries with gentler contractions.

Thus far, the analysis has dealt with the behaviour of the steady flow at low Reynolds number. In the next section, we investigate how the stability of the flow responds as Reynolds numbers are increased.

### 4.2. *Instability*

In many pipe flow applications, the transition to turbulence is generally observed to commence at Reynolds numbers of approximately 2300 (White 1999); however, under carefully controlled conditions the laminar regime can be maintained until much higher Reynolds numbers (Durst & Unsal 2006). Nonetheless, with the addition of a contraction, one would expect a somewhat lower threshold for stability. In this section, we deal firstly with a linear stability analysis, followed by an investigation of how this relates to experimental flows.

#### 4.2.1. *Linear stability analysis*

Figure 10 shows converged non-dimensional growth rates corresponding to the dominant linear instability mode for $b = 0.5$, 0.6, 0.75 and 0.9, derived from the linear stability analysis described in § 3.1. For $b = 0.75$ and 0.9, we see that the most unstable azimuthal mode number is $m = 1$. In these cases, the flow becomes critical at critical Reynolds number $Re_c = 770$ and 395, respectively. For $b = 0.9$, the higher mode numbers fall away more rapidly than in the case of $b = 0.75$. This is a trend which continues as the stenosis degree decreases; the shapes of the stability curves change, with the higher mode numbers becoming more unstable. Indeed, for $b = 0.5$

https://doi.org/10.1017/S0022112008004084 Published online by Cambridge University Press

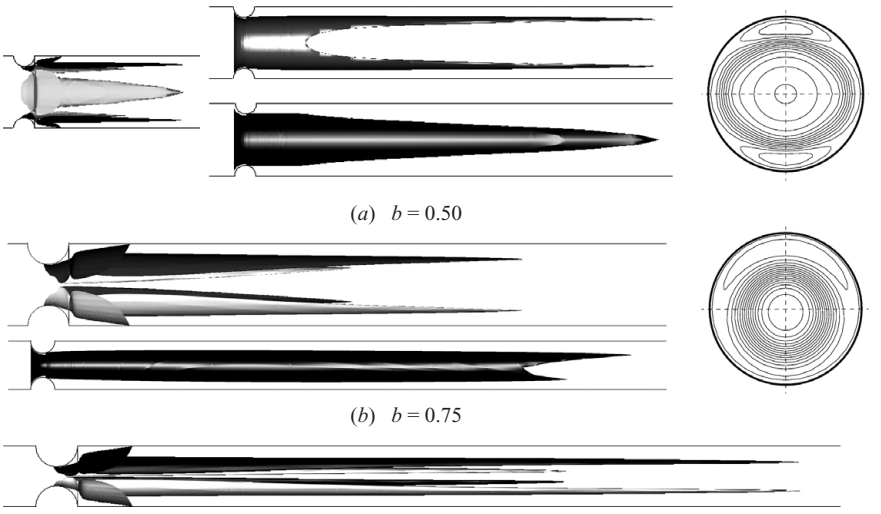



FIGURE 11. Plots of the most critical modes: (*a*) For $b = 0.5$, $Re = 2400$, at left, positive and negative isosurfaces of the streamwise vorticity of the most unstable perturbation mode ($m = 2$); middle, top and side views of an isosurface of the azimuthal vorticity for a linear combination of the base flow and the perturbation mode; and at right, contours of axial velocity for a cross-section taken at $z = 6/D$. (*b*) For $b = 0.75$, $Re = 800$, top and left, isosurfaces of the streamwise vorticity of the most unstable perturbation mode ($m = 1$); bottom, azimuthal vorticity of a combination of the base flow and mode; and at right, contours of the axial velocity for a cross-section at $z = 12/D$. (*c*) For $b = 0.9$, $Re = 400$, isosurfaces of the streamwise vorticity of the most unstable perturbation mode ($m = 1$).

and 0.6, the most unstable mode number is $m = 2$, the flow becoming critical at $Re_c = 2350$ and 1540, respectively.

Figure 11 depicts the structures of the unstable modes. The most unstable mode for $b = 0.50$, being of mode number $m = 2$, differs substantially from the other two cases presented, those being of mode number $m = 1$. The structure of the leading mode for $b = 0.75$, shown in figure 11(*b*), matches closely that reported by Sherwin & Blackburn (2005) for a similar geometry, consisting of a deflection of the jet from the tube centreline. Sherwin & Blackburn (2005) reported a critical Reynolds number value of 722, compared with the present value of 770. The difference in critical Reynolds number between the two cases can be attributed to the different geometries used in each case. The shorter stenosis length of the geometry used in the current study causes a more abrupt contraction of the flow, providing a marginally severer disruption to the flow than the smoother geometry of Sherwin & Blackburn (2005). The mode for $b = 0.9$ (see figure 11*c*) is essentially of the same form as for $b = 0.75$. The action of the perturbation – a shifting of the jet away from the axis of symmetry – bears some similarity to the symmetry-breaking bifurcation observed for flows in sudden expansions of two-dimensional channels (Drikakis 1997). In such flows, for a critical Reynolds number, the flow attaches strongly to one side of the channel immediately downstream of the expansion; the loss of axisymmetry caused by the leading $m = 1$ mode of the present work (figure 11*b*) is a milder example of this bifurcation.

For $b = 0.75$ and 0.9, the leading mode, $m = 1$, consists of a loss of symmetry of the jet downstream of the stenosis; for $b = 0.5$ the perturbation flow pinches the jet emanating from the contraction (see figure 11*a*); the centreline of the jet remains

https://doi.org/10.1017/S0022112008004084 Published online by Cambridge University Press

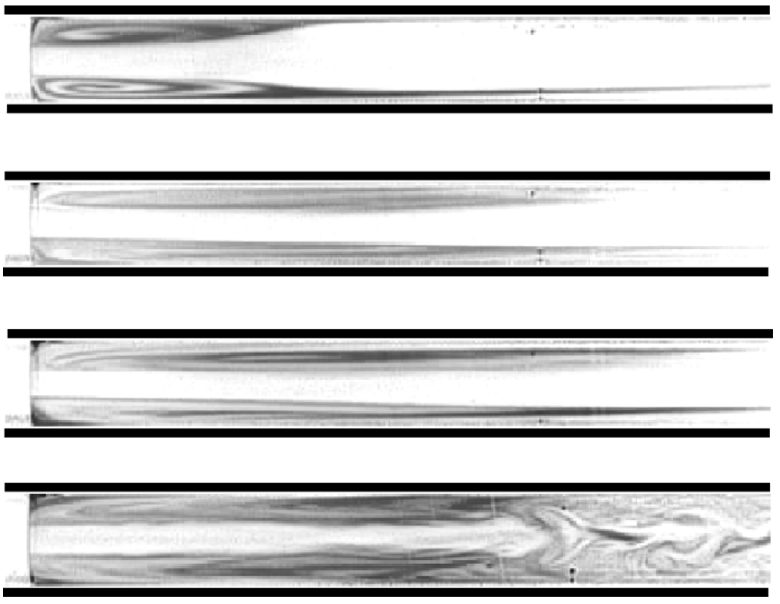


FIGURE 12. Dye visualizations at $b = 0.9$ and $Re =$ 42, 95, 135 and 194, from top to bottom. The positions of the walls have been superimposed. The area shown is immediately downstream of the non-transparent stenosis section, which is visible at the left of the figure.

undeflected. In summary, for high stenosis degree, the perturbation consists of a deflection or deviation of the jet from the tube centreline, while for lower stenosis degree, it consists of a pinching or flattening centred on the centreline. Taken up in the next section is the question of how this analysis compares with the stability of the flow in the experiments.

4.2.2. *Instability: experimental*

In contrast to the numerical simulations, all the results taken under experimental conditions were inevitably subject to some level of noise, be it originating from the environment or from imperfections in the construction of the rig. Another important difference from the numerical investigation is the nature of the stability analysis of § 3.1, which only relates to absolute stability. In the experiment, the presence of noise, combined with the long, thin shear layers which characterize the types of flow under investigation here, leads to the strong probability of convective instability playing a role in the stability of the flow.

As already shown, the length of the recirculation zone increases linearly with the Reynolds numbers. However, the stability of the experimental flow differs markedly from that predicted by linear stability analysis of the numerically simulated flow. Figure 12 shows dye visualizations for a range of Reynolds numbers, at $b = 0.9$. At low Reynolds number, the flow is steady and matches closely the numerical results. But as seen in the fourth image of figure 12 and as can be seen across the three stenosis degrees tested, at sufficiently high Reynolds numbers the flow becomes unstable. This instability, seemingly of a Kelvin–Helmholtz type, consists of small waves developing in the shear layer, propagating downstream and resulting in a breakdown, usually approximately four to five diameters downstream. In such cases, the end of the recirculation zone is no longer apparent, bearing some similarity to the flapping of

https://doi.org/10.1017/S0022112008004084 Published online by Cambridge University Press

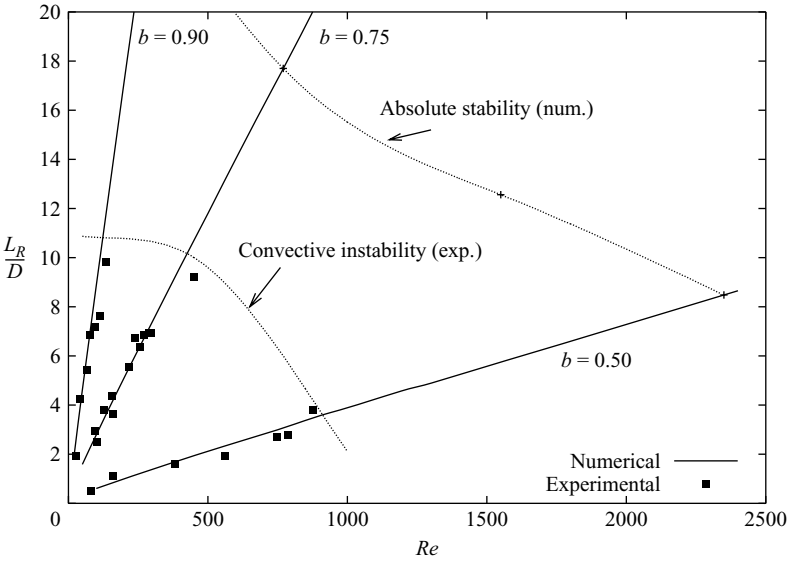



FIGURE 13. Description of boundaries of stability, as well as a comparison of experimental results to numerical. Solid black squares represent lengths taken from dye visualizations.

the recirculation zone seen behind a bump in an open flow (Marquillie & Ehrenstein 2003). Interestingly, the shear layer waves in the fourth image of figure 12 appear to not be strong enough to even form a clearly identifiable rolled-up vortex typical of a Kelvin–Helmholtz instability; rather the shear layer seems to gently undulate, before reaching a region of far stronger unsteadiness four to five diameters downstream.

The boundary at which this instability manifests is shown as the dotted line in figure 13, marked as 'convective instability (exp.)'. Below this boundary is also plotted a comparison between the numerically determined recirculation lengths and those measured from the experiment, using the dye visualizations. The results show a good agreement, up to the point at which convective instability sets in, which is not accounted for in the numerical simulations. However, this boundary will depend at least to some degree on the level of background noise in the experimental apparatus.

For $b = 0.75$, the boundary for convective instability in the flow, at $Re \approx 400$, is near its expected location, given the critical Reynolds numbers predicted in other experimental studies of steady stenotic flows. At $Re = 500$, Ahmed & Giddens (1983*b*) observed velocity oscillations of discrete frequencies but made no mention of any turbulence. The lower Reynolds number for convective instability in the present work may be attributed to the shorter stenosis length of the geometry. At $Re = 1000$, however, Ahmed & Giddens (1983*b*) noted in addition a region of turbulence for $z/D > 4$. In relation to the present work, one would expect that the velocity oscillations of discrete frequency seen in Ahmed & Giddens (1983*b*) would correspond with the type of convective instability seen above the boundary plotted in figure 13. Indeed, what could be described as turbulence with any certainty only appeared in flows of Reynolds numbers somewhat higher than the boundary for convective instability.

What figure 13 highlights is that experimentally the instability seen in the shear layer plays a major role in the transition of the flow from a steady state. Hence, the instability modes shown in figure 11 were never visible in the experiments. It is possible that they were present, despite the unsteadiness and irregularity caused by

https://doi.org/10.1017/S0022112008004084 Published online by Cambridge University Press

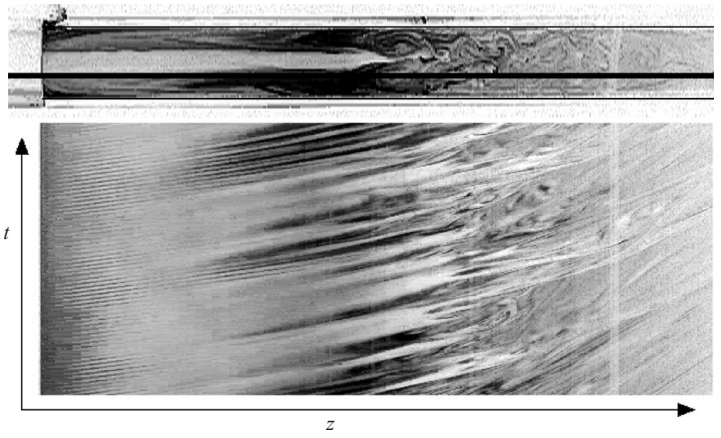



FIGURE 14. At top, the unsteady flow at $b = 0.9$, $Re = 194$. The spatio-temporal diagram, at bottom, is constructed using a single line of pixels taken from the long, black line in the top image. The waves seen in the shear layer are evident as straight lines to the left of the lower diagram.

the shear layer instability but were undetectable by our experimental methods. At the critical Reynolds numbers predicted numerically, experimental flows showed large convective growth of shear layer modes, leading to strong turbulence a short distance downstream of the stenosis.

The instability, seemingly convective in nature, warrants further analysis. Figure 14 shows, first, an image from a film of a dye visualization at $b = 0.9$ for $Re = 194$. The shear layer emanating from the stenosis appears to be parallel to the direction of the tube. The waves in the shear layer are just apparent downstream of the stenosis, while the large breakdown of the flow and the recirculation zone is evident at approximately five diameters downstream. The second image in the figure is a spatio-temporal diagram, constructed using a single line of pixels along the long, black straight line in the first image and by collecting the same line from each frame of the film. In this way, the waves in the shear layer can be seen as straight lines to the left of the diagram. Some of the shear layer waves propagate the entire length of the shear layer; many quickly peter out, while several appear to combine into larger waves, which are observable right up to the beginning of the strongly unsteady area. The irregular behaviour and strength of the shear layer waves indicate that the flow is highly sensitive and also points to the possible presence of a non-uniform noise.

Using such spatio-temporal diagrams, the period of the waves can be measured and a non-dimensionalized period, $T$, calculated according to

$$T = \frac{T_D \overline{U}}{D}, \tag{4.4}$$

where $T_D$ refers to the measured dimensional time of the period, which was always measured as close to the stenosis as possible, usually one to two diameters downstream of the stenosis. These non-dimensional periods are plotted in figure 15. In cases near the threshold of instability, oscillation periods were measured from flows that did not always display sustained unsteadiness; in this way, datum points were obtained at the lowest possible Reynolds numbers. Therefore, the boundaries in figures 13 and 15 do not necessarily align with each other. We see that across the three stenoses tested, the non-dimensionalized period of this instability remains roughly constant, particularly

https://doi.org/10.1017/S0022112008004084 Published online by Cambridge University Press

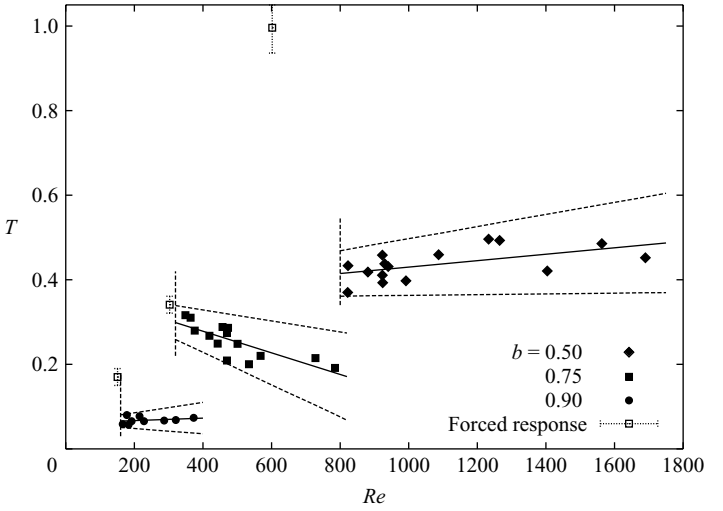



FIGURE 15. Measured instability periods across the stenosis degrees tested experimentally. The hollow boxes indicate the period at which forcing produces the greatest response in the flow, while vertical dotted lines show the lower limit at which a period of oscillation is able to be measured. Also included are 95 % confidence limits for each of the three datum sets.

in the cases corresponding to $b = 0.5$ and 0.9. However, the datum set at $b = 0.75$ appears to show a small decrease in period as the Reynolds number is increased. No physical mechanism that might explain this difference is immediately obvious; also plotted in figure 15 are lines of the best linear fits for the three datum sets, as well as 95% confidence intervals. The configuration of the intervals for the datum set at $b = 0.75$ leaves open the possibility that the period of the instability is still roughly constant with Reynolds number at $b = 0.75$.

In order to better understand the observed shear layer behaviour, the focus is now moved to those stable and steady flows that rest just below the threshold for convective instability, which is described in figure 13. To this end, the piston, as outlined in § 3, was employed in the experimental rig. Setting the piston motion to a very small amplitude of oscillation allows us to examine nominally stable flows just below the threshold of instability that are subjected to a periodic excitation. The three flows considered here ($b = 0.5$ and $Re = 600$; $b = 0.75$ and $Re = 300$; $b = 0.9$ and $Re = 150$) are chosen because experimentally they are steady and do not exhibit any apparent convective instability. All three flow configurations are not only stable but also strongly so, always returning quickly to steady state after any sort of disturbance. In this way, any response observed in the shear layer can be attributed without hesitation to the motion of the piston. The response consists of waves in the shear layer, which die away further downstream; the waves correspond to the frequency of the forcing. This results in no major breakdown of the flow, such as that seen in figure 14. The forcing of the piston is sinusoidal, and the amplitude is kept constant across the frequency range for each stenosis degree. The amplitude is chosen to be strong enough to excite a response in the shear layer sufficiently large to be seen and measured; generally, flows for $b = 0.5$ and $Re = 600$ required an amplitude of forcing of approximately $A = 0.04$, while for $b = 0.9$ and $Re = 150$, the amplitude was approximately $A = 0.01$.

After a general idea of the peak forcing frequency is obtained, a more exact value can be determined. The method used relies on the oscillation of the boundary between

https://doi.org/10.1017/S0022112008004084 Published online by Cambridge University Press

the dye of the recirculation zone and the clear fluid of the mainstream flow acting as an indicator of the response amplitude. Firstly, a smaller forcing amplitude is chosen, to avoid (nonlinear) roll-up; in this way, the stable flow configuration is retained as far as possible. Then the flow is filmed over a single run, with the forcing begun at a period known to be less than the non-dimensional period $T_p$ and slowly increased to a value known to be greater than $T_p$. A spatio-temporal diagram showing the oscillation in the shear layer at a single axial location is constructed, which shows the variation of the response amplitude with forcing frequency. This provides an accurate indicator of the peak forcing period. The three non-dimensional periods, $T_p$, found for each flow configuration are plotted as hollow boxes in figure 15.

All three values of $T_p$ are higher than the corresponding measured periods of the self-sustaining shear layer oscillations of the higher Reynolds number flows. Only in the case of $b = 0.75$ do the measured oscillation periods exhibit a trend towards the value of $T_p$; for the other two stenosis degrees, $T_p$ is significantly greater.

The action of the piston can be reproduced numerically. Perturbations of different frequencies and amplitudes can be applied at the flow inlet. In many simulations, this produces a disturbance in the flow which is not apparent to the naked eye; however, with the entire velocity field known, the response to the forcing can be accurately measured. This is achieved by calculating the maximum (over one period of the perturbation) of the kinetic energy over the domain of the velocity field of the perturbed flow minus the velocity field of the unperturbed base flow, of the form

$$E' = 0.5 \int\int r(\overline{\boldsymbol{u}} - \overline{\boldsymbol{u}}_{base})^2 \, \mathrm{d}r \, \mathrm{d}z. \tag{4.5}$$

Normalized by the kinetic energy of the unperturbed base flow ($E = \int\int r(\overline{\boldsymbol{u}}_{base})^2 \, \mathrm{d}r \, \mathrm{d}z$), this provides a measure of the disturbance caused by the forcing, even for cases in which the excited response is very small.

In order to examine the effect of different forcing amplitudes, figure 16($a$) presents the responses over a range of forcing periods of numerical simulations of the flow for $b = 0.9$ and $Re = 150$, $b = 0.75$ and $Re = 300$ and $b = 0.5$ and $Re = 600$. The three sets of results producing the largest responses are from simulations run with the same forcing amplitude employed in the experiment ($A = 0.01$ for $b = 0.9$; $A = 0.025$ for $b = 0.75$; and $A = 0.04$ for $b = 0.5$). Further simulations run for the three cases with amplitudes $A = 0.01$, 0.001 and 0.0001 show the variation of the response with forcing amplitude. Below an amplitude of $A = 0.01$, there is only a minimal change in the response profile. Figure 16($b$) plots the peak forcing periods $T_p$ for each case, as functions of amplitude. The variation of the peak forcing period with amplitude is minimal, although there is a small increase as the forcing amplitude is increased to the values used experimentally. For those amplitudes, only the peak period of the case of $b = 0.5$ and $Re = 600$ falls close to the error margins of the corresponding experimental result.

From figure 16($b$), for $Re = 600$, $b = 0.5$ and $A = 0.04$, the period which excites the greatest response in the flow is $T_p = 0.93$, compared with the value calculated from the experimental dye visualizations of $T_p = 1$. For stenosis degrees $b = 0.75$ and $b = 0.9$, the comparison with the experimentally determined peak forcing periods is not as strong. Interestingly, the experimental result for the peak forcing period of 0.34 for $b = 0.75$, $Re = 300$ and $A = 0.025$ falls closer to the numerically determined peak forcing period for the smaller forcing amplitudes than for the period for $A = 0.25$. The period of peak response of $T_p = 0.097$ for 0.9 and $Re = 150$ does not match as closely with the experimentally measured value of 0.17.

https://doi.org/10.1017/S0022112008004084 Published online by Cambridge University Press

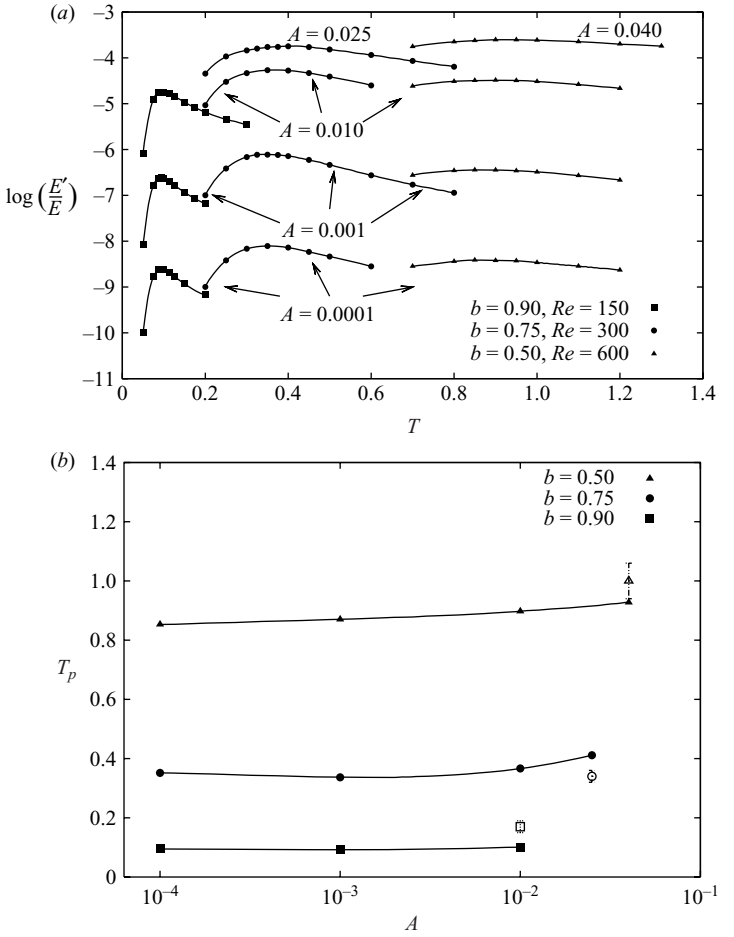



FIGURE 16. (*a*) Plots of the domain integral, $E'/E$, of the perturbed flow minus the base flow against the period of the forcing, $T$, calculated for the three cases tested experimentally: $b = 0.9$, $Re = 150$ and $A = 0.01$; $b = 0.75$, $Re = 300$ and $A = 0.025$; $b = 0.5$, $Re = 600$ and $A = 0.04$. Also included are results from simulations run with the same parameters but with a smaller forcing amplitudes of $A = 0.01$, 0.001 and 0.0001. (*b*) Variation of the peak forcing periods, $T_p$, with forcing amplitude (numerical) for the three cases considered. The three experimentally determined forcing periods are plotted in hollow symbols.

To examine the change in the peak forcing period with the Reynolds numbers, a uniform forcing amplitude of $A = 0.001$ is chosen. As can be seen from figure 16(*b*), the change in response profile as the forcing amplitude is reduced further is minimal. Figure 17 plots the response $E'/E$ against forcing period, $T$, across several Reynolds numbers and for stenosis degrees of $b = 0.5$, 0.75 and 0.9. For each stenosis degree tested, as the Reynolds number is increased, the response increases exponentially; however, the behaviour of the response curve does not change significantly. It is only for higher Reynolds numbers that the curve changes, and the values of $T_p$ increase, as can be seen in the inset figures. In figure 17(*b*), the flows for $b = 0.75$ exhibit only slightly smaller peak forcing periods than those observed in Blackburn & Sherwin (2007) for their steady flow through a stenosis of longer length. This is likely due to the more abrupt nature of the blockage in the present geometry, which causes a greater

https://doi.org/10.1017/S0022112008004084 Published online by Cambridge University Press

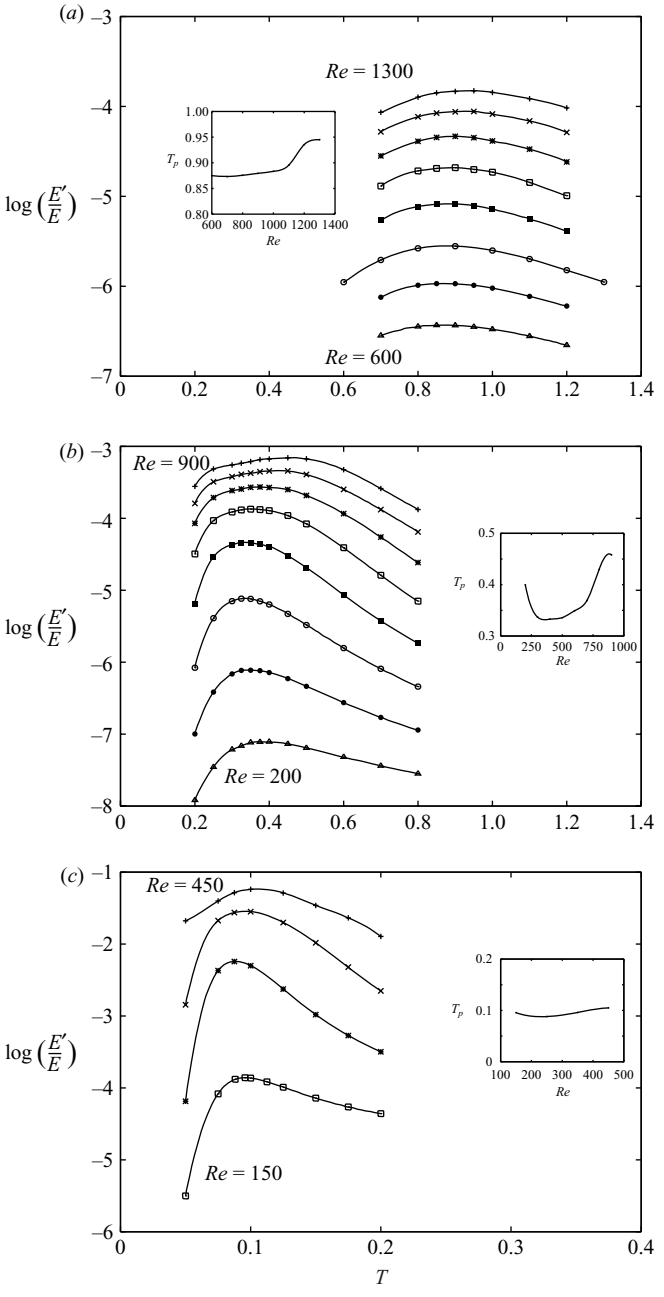



FIGURE 17. Plots of the domain integral, $E'/E$, of the perturbed flow minus the base flow against the period of the forcing, $T$, calculated for numerical simulations at a range of Reynolds numbers (at intervals of 100) across three stenosis degrees, (*a*) $b = 0.5$, (*b*) $b = 0.75$ and (*c*) $b = 0.9$, all with forcing amplitude $A = 0.001$. Inset are plots of the variation of the period producing the greatest response, $T_p$, with Reynolds number.

acceleration of the flow. This greater acceleration results in thinner downstream shear layers, which in turn respond more to higher frequency forcings.

In summary, the forcing period at which the shear layer of flows in the stable regime responds most strongly is higher than the period of oscillation of shear layer

https://doi.org/10.1017/S0022112008004084 Published online by Cambridge University Press

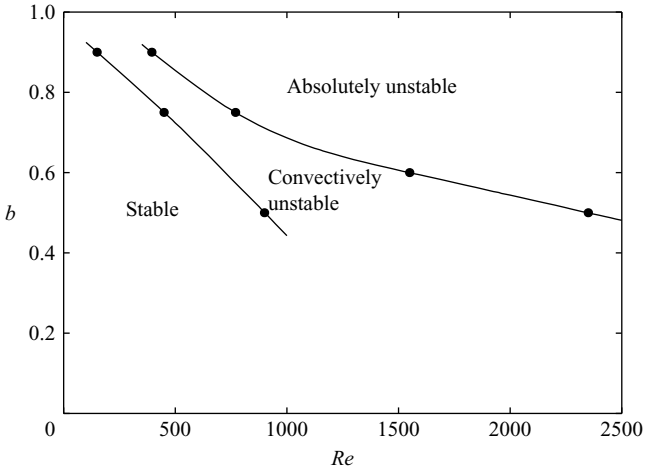



FIGURE 18. Map of the flow stability throughout the parameter space. The lower boundary denotes the convective instability seen experimentally, while the upper boundary is taken from linear stability analysis of the numerically derived flows.

waves seen in convectively unstable flows of higher Reynolds number. The most obvious difference between the two generic flows either side of the stability boundary is the existence in one flow of an area of strong unsteadiness four to five diameters downstream of the stenosis, and its absence in the other. In the cases in which a steady flow is forced, the excitation is evident in perturbations in the shear layer just downstream of the stenosis. These perturbations or waves then die away, with the flow remaining steady and unperturbed further downstream. However, when dealing with the unforced flows of higher Reynolds number, the equivalent waves of the self-sustained instability seen in the shear layer travel the length of the recirculation, the end of which is detached and free from the wall, lost somewhere amongst the breakdown of the flow, as seen in figure 14. It is possible that this area of turbulence is the source of the higher frequency perturbations seen in the convectively unstable flows. A nonlinear feedback from the downstream turbulence may be altering the noise profile to which the flow is normally subject in the experiment. In this scenario, the uneven excitation of the shear layer results in what would normally be the most dominant frequency being overtaken by others. Such an explanation would also account for the roughly constant period of shear layer oscillation seen at higher Reynolds number.

## 5. Conclusions

A study of the steady flow through a simplified stenotic geometry of varying stenosis degree has been presented. The flow consists of a jet emanating from the contraction and then expanding downstream, creating a recirculation zone directly behind the stenosis. Numerically, it was found that the length of the recirculation zone downstream of the stenosis varies linearly with Reynolds number, while for a given stenosis degree, similarity was found to exist between flows of different Reynolds number. By drawing an analogy with the flow around a circular cylinder in a free stream for low Reynolds number, a good collapse of the recirculation lengths was obtained. This suggests that the reattachment length behaves similar to the recirculation zone found in the wake of a circular cylinder at low Reynolds number.

https://doi.org/10.1017/S0022112008004084 Published online by Cambridge University Press

Linear stability analysis identified unstable azimuthal modes of wavenumber $m = 1$ for the stenosis degrees $b = 0.75$ and 0.9, with critical Reynolds numbers 770 and 395, respectively. For $b = 0.5$, the most unstable mode is for $m = 2$, the instability mode taking a different structure as the stenosis degree changes. Experimentally, a different instability was found to be dominant, consisting of a convectively amplified perturbation in the shear layer, growing and causing breakdown of the flow four to five diameters downstream. A summary of the limits of stability investigated in this study is given in figure 18. The period of these perturbations just downstream of the stenosis was measured and, using the non-dimensionalization $T = T_D\overline{U}/D$, shown to be roughly constant at higher Reynolds numbers. Stable flows, both numerical and experimental, when subjected to small-amplitude forcing, respond most for forcing periods higher than those measured in the unsteady experimental flows at higher Reynolds numbers. The existence of nonlinear feedback between turbulent flow downstream and the unstable shear layer upstream was put forward as a possible explanation for this phenomenon.

The authors thank Jérôme Hœpffner for many useful discussions and insights. The authors gratefully acknowledge financial support from the Australian Research Council (ARC Discovery Project Grant DP0555897 and ARC Linkage International Grant LX0668992), the Australian Academy of Science and the Embassy of France in Australia. M. D. Griffith would also like to acknowledge the assistance of a postgraduate publication award from the Monash Research Graduate School.

## REFERENCES

Ahmed, S. A. 1998 An experimental investigation of pulsatile flow through a smooth constriction. *Expl Therm. Fluid Sci.* **17**, 309–318.

Ahmed, S. A. & Giddens, D. P. 1983*a* Flow disturbance measurements through a constricted tube at moderate Reynolds numbers. *J. Biomech.* **16**, 955–963.

Ahmed, S. A. & Giddens, D. P. 1983*b* Velocity measurements in steady flow through axisymmetric stenoses at moderate Reynolds numbers. *J. Biomech.* **16**, 505–516.

Ahmed, S. A. & Giddens, D. P. 1984 Pulsatile poststenotic flow studies with laser doppler anemometry. *J. Biomech.* **17**, 695–705.

Blackburn, H. M. & Sherwin, S. J. 2007 Instability modes and transition of pulsatile stenotic flow: pulse–period dependence. *J. Fluid Mech.* **573**, 57–88.

Cassanova, R. A. & Giddens, D. P. 1978 Disorder distal to modified stenoses in steady and pulsatile flow. *J. Biomech.* **11**, 441–453.

Deplano, V. & Siouffi, M. 1999 Experimental and numerical study of pulsatile flows through stenosis: wall shear stress analysis. *J. Biomech.* **32**, 1081–1090.

Drikakis, D. 1997 Bifurcation phenomena in incompressible sudden expansion flows. *Phys. Fluids* **9**, 76–87.

Durst, F. & Unsal, B. 2006 Forced laminar-to-turbulent transition of pipe flows. *J. Fluid Mech.* **560**, 449–464.

Griffith, M. D. 2007 The stability and behaviour of flows in stenotic geometries. PhD thesis, Department of Mechanical & Aerospace Engineering, Monash University, Melbourne, Australia.

Griffith, M. D., Thompson, M. C., Leweke, T., Hourigan, K. & Anderson, W. P. 2007 Wake behaviour and instability of flow through a partially blocked channel. *J. Fluid Mech.* **582**, 319–340.

Karniadakis, G. E., Israeli, M. & Orszag, S. A. 1991 High-order splitting methods of the incompressible Navier–Stokes equations. *J. Comput. Phys.* **97**, 414–443.

Ku, D. N. 1997 Blood flow in arteries. *Annu. Rev. Fluid Mech.* **29**, 399–434.

Long, Q., Xu, X. Y., Ramnarine, K. V. & Hoskins, P. 2001 Numerical investigation of physiologically realistic pulsatile flow through arterial stenosis. *J. Biomech.* **34**, 1229–1242.

https://doi.org/10.1017/S0022112008004084 Published online by Cambridge University Press

Mallinger, F. & Drikakis, D. 2002 Instability in three-dimensional, unsteady, stenotic flows. *Intl J. Heat Fluid Flow* **23**, 657–663.

Marquillie, M. & Ehrenstein, U. 2003 On the onset of nonlinear oscillations in a separating boundary-layer flow. *J. Fluid Mech.* **490**, 169–188.

Ohja, M., Cobbold, R. S. C., Johnston, K. W. & Hummel, R. L. 1989 Pulsatile flow through constricted tubes: an experimental investigation using photochromic tracer methods. *J. Fluid Mech.* **203**, 173–197.

Sheard, G. S., Thompson, M. C. & Hourigan, K. 2003 From spheres to circular cylinders: classification of bluff ring transitions and structure of bluff ring wake. *J. Fluid Mech.* **492**, 147–180.

Sherwin, S. J. & Blackburn, H. M. 2005 Three-dimensional instabilities of steady and pulsatile axisymmetric stenotic flows. *J. Fluid Mech.* **533**, 297–327.

Stroud, J. S., Berger, S. A. & Saloner, D. 2000 Influence of stenosis morphology in flow through severely stenotic vessels: Implications for plaque rupture. *J. Biomech.* **33**, 443–455.

Stroud, J. S., Berger, S. A. & Saloner, D. 2002 Numerical analysis of flow through a severely stenotic carotid artery bifurcation. *J. Biomech. Engng* **124**, 9–19.

Taneda, S. 1956 Experimental investigation of the wakes behind cylinders and plates at low Reynolds numbers. *J. Phys. Soc. Japan* **11**, 302–307.

Thompson, M. C., Hourigan, K. & Sheridan, J. 1996 Three-dimensional instabilities in the wake of a circular cylinder. *Expl Therm. Fluid Sci.* **12**, 190–196.

Thompson, M. C., Leweke, T. & Provansal, M. 2001 Kinematics and dynamics of sphere wake transition. *J. Fluids Struct.* **15**, 575–585.

Varghese, S. S., Frankel, S. H. & Fischer, P. F. 2007*a* Direct numerical simulation of stenotic flows. Part 1. Steady flow. *J. Fluid Mech.* **582**, 253–280.

Varghese, S. S., Frankel, S. H. & Fischer, P. F. 2007*b* Direct numerical simulation of stenotic flows. Part 2. Pulsatile flow. *J. Fluid Mech.* **582**, 281–318.

White, F. M. 1999 *Fluid Mechanics* (4th ed.). McGraw-Hill.

Wootton, D. M. & Ku, D. N. 1999 Fluid mechanics of vascular systems, diseases, and thrombosis. *Annu. Rev. Biomed. Engng* **1**, 299–329.

https://doi.org/10.1017/S0022112008004084 Published online by Cambridge University Press